Modelling Hadronic Matter

2016 J. Phys.: Conf. Ser. 706 032001

(http://iopscience.iop.org/1742-6596/706/3/032001)

Modelling Hadronic Matter

Débora P. Menezes
Departamento de Fsica, Universidade Federal de Santa Catarina, Florianpolis, Brazil
E-mail: `debora.p.m@ufsc.br`

Abstract. Hadron physics stands somewhere in the diffuse intersection between nuclear and particle physics and relies largely on the use of models. Historically, around 1930, the first nuclear physics models known as the liquid drop model and the semi-empirical mass formula established the grounds for the study of nuclei properties and nuclear structure. These two models are parameter dependent. Nowadays, around 500 hundred non-relativistic (Skyrme-type) and relativistic models are available in the literature and largely used and the vast majority are parameter dependent models. In this review I discuss some of the shortcomings of using non-relativistic models and the advantages of using relativistic ones when applying them to describe hadronic matter. I also show possible applications of relativistic models to physical situations that cover part of the QCD phase diagram: I mention how the description of compact objects can be done, how heavy-ion collisions can be investigated and particle fractions obtained and show the relation between liquid-gas phase transitions and the pasta phase.

1. Introduction and historical perspectives

Hadron physics is a field of studies that lies in between nuclear and particle physics, taking advantage of quantum field theory techniques. The ideal scenario for the investigation of hadron physics problems would be the use of quantum chromodynamics (QCD) solutions, which to date, are not feasible. One can rely on two possibilities: lattice QCD and effective theories. So far, lattice QCD presents results for a restricted space of the QCD phase diagram (zero or very low chemical potentials) [1] and hence, the use of effective models has been very important in advancing our knowledge in a wider scenario, where finite chemical potentials are present.

The nuclear physics modelling history started with two very simple models: the liquid drop model, introduced in 1929 [2] and the semi-empirical mass formula, presented in 1935 by Bethe and Weizsäcker [3]. Both models are so close to each other in basic ideas that their nomenclature is very often just mixed up.

The liquid drop model was developed from the observation that the nucleus has behavior and properties that resemble the ones of an incompressible fluid, such as:

- The nucleus has low compressibility due to its internal almost constant density;
- The nucleus presets well defined surface;
- The nucleus radius varies with the number of nucleons as $R = R_o A^{1/3}$, where $R_0 \simeq 1.2 \times 10^{-15}$ m;
- The nuclear force saturates and it is isospin independent.

A typical nuclear density profile is shown in Fig. 1, from where one can see that the density is almost constant up to a certain point and then it drops quite rapidly close to the surface, determining the nucleus radius.

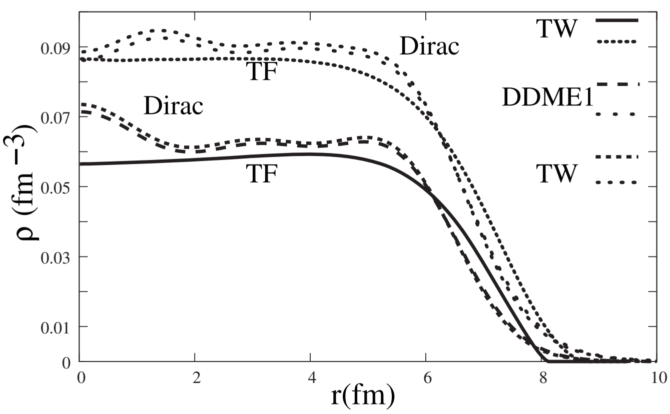

Figure 1. Neutron and proton density profiles obtained with two different methods (solution of the Dirac equation and the Thomas-Fermi approximation) and different models. Figure taken from [4].

The binding energy B of a nucleus ${}^A_Z X_N$ is given by the difference between its mass mc^2 and the mass of its constituents (Z protons and N neutrons):

$$B = (Zm_p + Nm_n - (m(^AX) - Zm_e))c^2 = (Zm(^1H) + Nm_n - m(^AX))c^2, \tag{1}$$

where $m(^AX)$ is the mass of the chemical element ^AX and is given in atomic mass units. The binding energy per nucleon $\frac{B}{A}$ is plotted in Fig. 2, from where one can see that the curve is relatively constant and of the order of $8,5$ MeV except for light nuclei. A successful attempt to reproduce this curve was made with the semi-empirical mass formula, which is a parameter dependent expression used to fit the experimental results. It is given by:

$$B(Z, A) = a_v A - a_s A^{\frac{2}{3}} - a_c e^2 \frac{Z(Z-1)}{A^{\frac{1}{3}}} - a_i \frac{(N-Z)^2}{A} + \delta(A). \tag{2}$$

The quantities in this expression refer to a volume term, a surface term, a Coulomb term, an energy symmetry term and a pairing interaction term. Details on how these terms where obtained are easily found in many textbooks. See, [5],[6], for instance. Of course, many parameterizations can be obtained from the fitting of the data. One possible set is $a_v = 15,68$ MeV, $a_s = 18,56$ MeV, $a_c \times e^2 = 0,72$ MeV, $a_i = 18,1$ MeV and

$$\delta = \begin{cases} 34 \ \ A^{-3/4} MeV, & \text{even-even nuclei,} \\ 0, & \text{even-odd nuclei,} \\ -34 \ \ A^{-3/4} MeV, & \text{odd-odd nuclei.} \end{cases} \tag{3}$$

Although very naive, these two models combined can explain many important nuclear physics properties. One example is nuclear fission, that depends on the balance between the Coulomb and the surface terms [5].

Other important subjects related to nuclear physics that can be explained by parameter dependent nuclear models is the fusion of elements in the stars and the primordial nucleosynthesis. The abundance of chemical elements in the observable universe is the following: 71% is Hydrogen, 27% is Helium, 1.8% are Carbon to Neonium elements, 0.2% are Neonium to Titanium, 0.02% is Lead and only 0.0001% are elements with atomic number larger than

Journal of Physics: Conference Series **706** (2016) 032001 doi:10.1088/1742-6596/706/3/032001

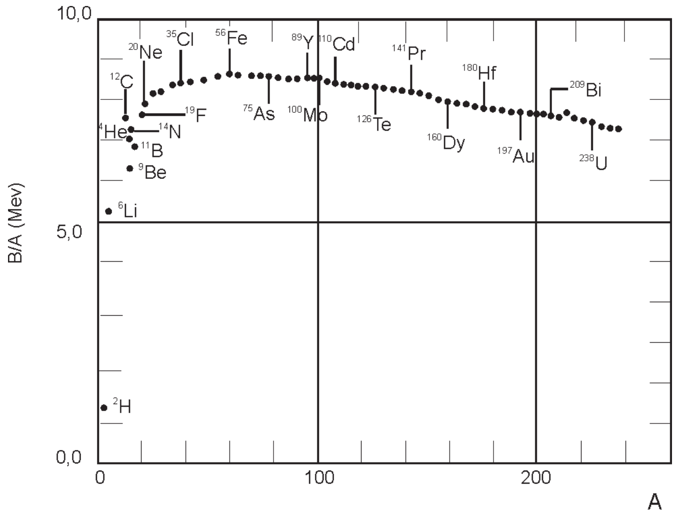

Figure 2. Binding energy per nucleon as a function of the number of nucleons. Figure taken from [5].

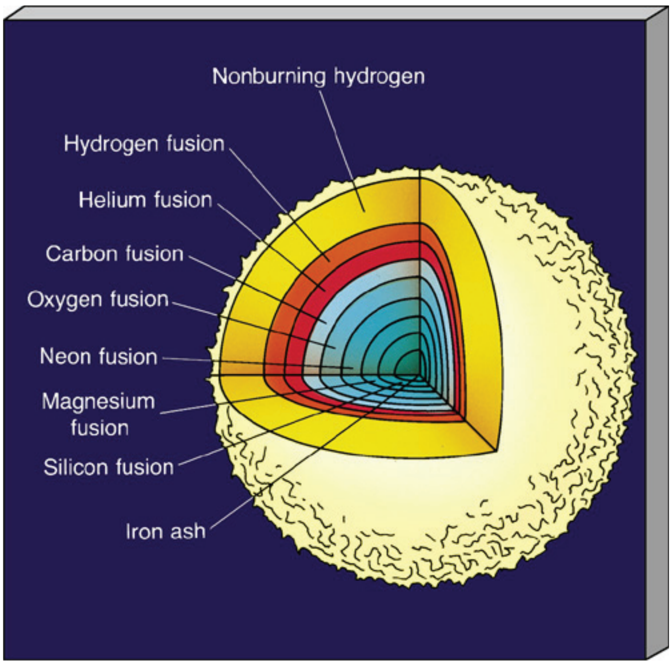

Figure 3. Possible chemical elements synthesized in stellar fusion.

60. If one looks at Fig. 2, it is easy to identify the element with the largest binding energy, which is ^{56}Fe. It is then, possible to explain why elements with atomic numbers $A \leq 56$ can be synthesized in the stars by nuclear fusion and heavier elements are only expected to be synthesized in supernova explosions. For a rough idea of the possible chains of fusion taking place in stars, one can look at Fig. 3.

Once the star is born, it takes sometime fusing all the chemical elements in its interior, until it dies. Depending on its mass, the death is more or less spectacular. According to the

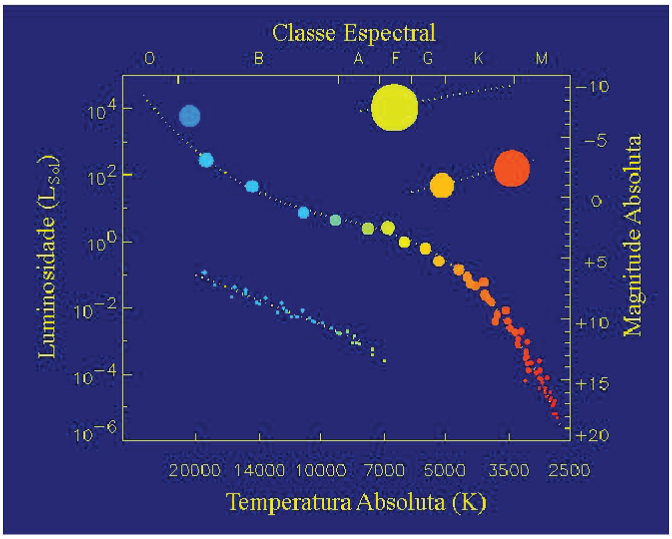

Figure 4. Hertzspring and Russel Diagram. Notice that the temperature increases from right to left.

Hertzspring and Russel (HR) diagram, depicted in Fig. 4, the star spends most of its time in the main sequence, the central line of the diagram. A star like the sun becomes a white dwarf after its death, shown at lower luminosities and higher temperatures, towards the left corner of the diagram. Stars with masses higher than 8 solar masses ($M_\odot$) become either a neutron star or a black hole and these compact objects are not shown in the HR Diagram for obvious reasons: they do not emit visible light waves and their luminosity is negligible or inexistent. Hadronic models can also be used to explain neutron stars properties and their internal constituents.

If one wants to have a broader view of the possible use of parameter dependent hadronic models, one should look at the QCD phase diagram, shown in Fig. 5. Low baryonic densities are related to low chemical potentials. As already stated, LQCD can only describe zero (or very low) chemical potential systems. For the understanding of the physics represented in the rest of the QCD diagram, effective hadronic models are an essential tool. Compact stars are cold objects with high internal baryon densities. In heavy ion collisions (RHIC/USA, LHC/CERN), matter is hot and baryon density is low. In experiments at FAIR (GSI, Germany) and NICA (Dubna, Russia), the baryon density is not too low and the temperatures not too high. Next, I discuss how we can choose or build appropriate models to tackle these specific problems.

2. Existing non-relativistic and relativistic models

From the development of the very first nuclear physics models, the main idea was to satisfy experimental values. In almost one century of research, the models became more and more sophisticated, but they remain valid if and only if nuclear bulk properties are satisfied. The most important of these properties are the binding energy, the saturation density, the symmetry energy, its derivatives and the incompressibility. One can easily notice that all of them are related to the semi-empirical mass formula given in Eq. (2). However, many different parameter sets can satisfy the same constraints, but what happens when one moves to higher densities or to finite temperature, situations present in the QCD phase diagram? A simple example of what happens is shown in Fig. 6 for some non-relativistic, Skyrme-type (SHF) and relativistic mean field (RMF) models. Although all models reproduce correctly the binding energy value at more or less the same saturation density and the incompressibility, which is a derivative of the energy

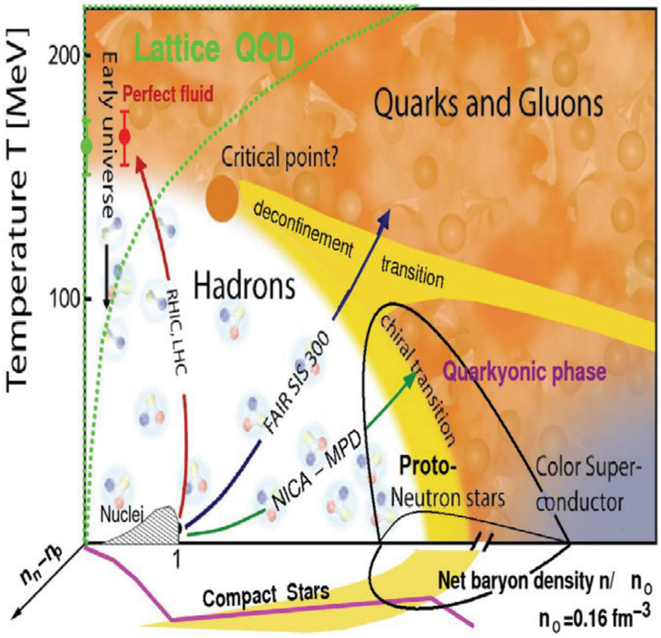

Figure 5. QCD phase diagram.

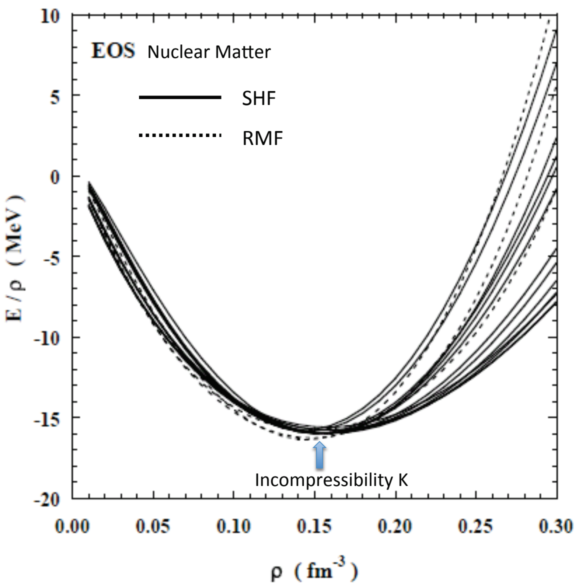

Figure 6. Binding energy as a function of baryon density for different Skyrme-type (SHF) and relativistic (RMF) models. This figure is a courtesy of Dr. Jirina Stone.

density acquires similar values also at the saturation density, once the density increases, they deviate considerably from each other.

In Fig. 7, an even broader pattern is seen if one looks at the symmetry energy. At the saturation point, again all models give approximately the same values, but at larger densities

$$\varepsilon_\delta(\rho) = \frac{1}{2}\lim_{I\to 0}\frac{\partial^2}{\partial I^2}\left(\frac{H_{nm}}{\rho}\right) \qquad \varepsilon_\delta(\rho) = J + \frac{L}{3}\frac{\rho-\rho_{nm}}{\rho_{nm}} + \frac{K_{sym}}{18}\left(\frac{\rho-\rho_{nm}}{\rho_{nm}}\right)^2.$$

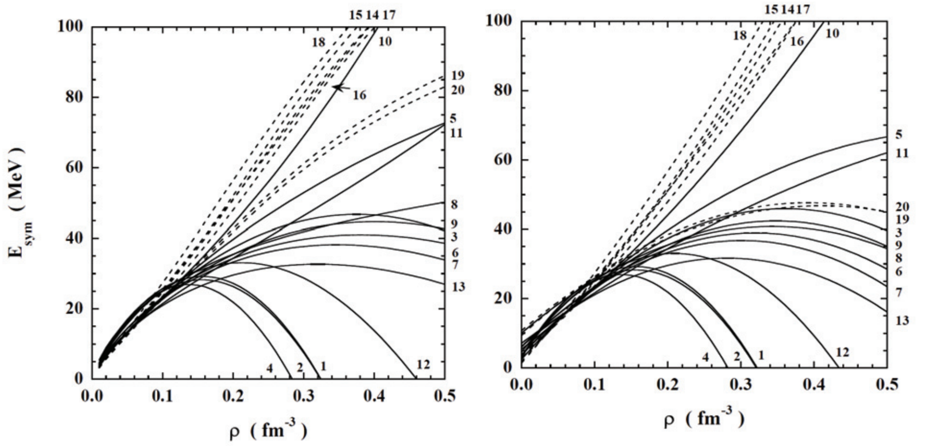

Figure 7. Symmetry energy as a function of the baryon density. The expressions relate the symmetry energy with its slope (L) and curvature (K_{sym}) and nm means nuclear matter. This figure is a courtesy of Dr. Jirina Stone.

anything is possible, from curves that increase to models that produce curves that decrease and even become zero at no so high baryon densities. So, how to choose one model? By choosing adequate constraints and checking whether the models satisfy them, as done is [7] for non-relativistic models and in [8] for relativistic ones.

An important constraint is the isospin symmetric nuclear matter incompressibility (or compression modulus) K_0. The incompressibility values can be inferred from experiment and from theory. Experimentally, results coming from giant resonances, mainly isoscalar giant monopole (GMR) and isovector giant dipole (GDR) resonances can be used. Theoretically, values for the incompressibility can be obtained with Hartree-Fock plus random-phase-approximation (RPA) calculations, for instance. A reasonable value, adopted in [8] is $K_0 = 230 \pm 40$ MeV.

The symmetry energy (J) and its slope (L_0) at the saturation density are also important constraints. Experimental data for the symmetry energy can be obtained from heavy-ion collisions, pygmy dipole resonances, isobaric analog states, GMR and GDR. A restricted band for the values of J ($25 < J < 35$ MeV) and L_0 ($25 < L_0 < 115$ MeV) based on 28 experimental and observational data is given in [9].

The volume part of the isospin incompressibility, known as $K_{\tau,\mathrm{v}}$, which depends on several liquid drop model quantities is also a constraint that can be used. When it is extracted from a simple fitting to GMR data, it includes not only volume, but also surface contributions and hence, its use is a bit more controversial. In [8] it was chosen to be $K_\tau = -550 \pm 150$ MeV.

With the help of the above mentioned constraints, 240 non-relativistic Syrme models and

263 relativistic mean field models were assessed, in describing nuclear matter up to 3 times nuclear saturation density. Out of the Skyrme-type models, 16 were approved [7] and out of the relativistic models, 35 were approved [8]. Of course, many other models also satisfy most of the constraints, but not all of them. Hence, when one model is chosen, a complete understanding of where it fails is possible. If one believes that his/her preferred model fails at satisfying constraints that he/she does not think important for the application that will be done, the use of the model can still be justified.

In what follows, I will just discuss results obtained with relativistic models because Skyrme-type models present some problems that I would like to avoid. The most common ones are: Many of the equations of state are only suited at low densities because they become a-causal; Non-relativistic models lead to symmetry energies that decrease too much after $3\rho_0$, as seen in Fig. 7, which is a very serious deficiency if we want to apply them to the study of neutron stars, a highly asymmetric system. Of course, these problems can be cured with the inclusion of three-body forces, but them the calculations become much more complicated. Relativistic models, on the other hand, are Lorentz invariant and generally causal; if they are extended to finite temperature systems, anti-particles appear naturally and, mesonic degrees of freedom are explicitly treated. Moreover, the very same models can be applied to describe the physics of different regions of the QCD phase diagram.

3. Relativistic models for astrophysical studies

Essential ingredients for astrophysical model calculations can be obtained from appropriate equations of state (EOS). Once the EOS are computed, they are used as input to the Tolman-Oppenheimer-Volkoff equations (TOV) [10], which yield as output some macroscopic stellar properties, as masses, radii and central energy densities. Other static properties, as the moment of inertia and rotation rate can also be inferred. The EOS are also used in calculations involving the dynamical evolution of supernova, protoneutron star evolution and cooling, conditions for nucleosynthesis and stellar chemical composition, transport properties and protoneutron star internal temperature.

So far, many detailed aspects have been extensively studied and are well-known as matter at zero temperature, symmetric nuclear and pure neutron matter, low density matter, including clusterization and the pasta phase, high density matter and matter in β-equilibrium. However, an EOS that covers the complete QCD phase diagram parameter space in (T, μ_B) in a single model still requires improvements. To date, there are just a few of these EOS and the CompOSE (CompStar Online Supernovae Equations of State) [11] is the result of the effort of many nuclear physicists to provide astrophysicists with reliable EOS ready to be used in numerical simulations.

Having motivated the use of relativistic models, one example of a complete Lagrangian density that describes baryons interacting among each other by exchanging scalar-isoscalar (σ) , vector-isoscalar (ω) vector-isovector (ρ) and scalar-isovector (δ) mesons is the following:

$$\mathcal{L}_{\rm NL} = \mathcal{L}_{\rm bm} + \mathcal{L}_\sigma + \mathcal{L}_\omega + \mathcal{L}_\rho + \mathcal{L}_\delta + \mathcal{L}_{\sigma\omega\rho}, \tag{4}$$

where

$$\mathcal{L}_{\rm bm} = \sum_b \overline{\psi_b}(i\gamma^\mu\partial_\mu - M_b)\psi_b + g_{\sigma b}\sigma\overline{\psi_b}\psi_b - g_{\omega b}\overline{\psi_b}\gamma^\mu\omega_\mu\psi_b - \frac{g_{\rho b}}{2}\overline{\psi_b}\gamma^\mu\vec{\rho}_\mu\vec{\tau}\psi_b + g_{\delta b}\overline{\psi_b}\vec{\delta}\vec{\tau}\psi_b, \tag{5}$$

$$\mathcal{L}_\sigma = \frac{1}{2}(\partial^\mu\sigma\partial_\mu\sigma - m_\sigma^2\sigma^2) - \frac{A}{3}\sigma^3 - \frac{B}{4}\sigma^4, \tag{6}$$

$$\mathcal{L}_\omega = -\frac{1}{4}F^{\mu\nu}F_{\mu\nu} + \frac{1}{2}m_\omega^2\omega_\mu\omega^\mu + \frac{C}{4}(g_\omega^2\omega_\mu\omega^\mu)^2, \tag{7}$$

$$\mathcal{L}_\rho = -\frac{1}{4}\vec{B}^{\mu\nu}\vec{B}_{\mu\nu} + \frac{1}{2}m_\rho^2\vec{\rho}_\mu\vec{\rho}^\mu, \tag{8}$$

$$\mathcal{L}_\delta = \frac{1}{2}(\partial^\mu\vec{\delta}\partial_\mu\vec{\delta} - m_\delta^2\vec{\delta}^2), \tag{9}$$

and

$$\begin{aligned}\mathcal{L}_{\sigma\omega\rho} &= g_\sigma g_\omega^2 \sigma\omega_\mu\omega^\mu\left(\alpha_1 + \frac{1}{2}\alpha_1{}' g_\sigma\sigma\right) + g_\sigma g_\rho^2\sigma\vec{\rho}_\mu\vec{\rho}^\mu\left(\alpha_2 + \frac{1}{2}\alpha_2{}' g_\sigma\sigma\right)\\ &+ \frac{1}{2}\alpha_3{}' g_\omega^2 g_\rho^2\omega_\mu\omega^\mu\vec{\rho}_\mu\vec{\rho}^\mu.\end{aligned} \tag{10}$$

In this Lagrangian density, $\mathcal{L}_{\rm bm}$ stands for the kinetic part of the baryons added to the terms representing the interaction between them and mesons σ, δ, ω, and ρ. The term $\mathcal{L}_j$ represents the free and self-interacting terms of the meson j, for $j = \sigma, \delta, \omega$, and ρ. The last term, $\mathcal{L}_{\sigma\omega\rho}$, takes into account crossing interactions between the meson fields. The antisymmetric field tensors $F_{\mu\nu}$ and $\vec{B}_{\mu\nu}$ are given by $F_{\mu\nu} = \partial_\nu\omega_\mu - \partial_\mu\omega_\nu$ and $\vec{B}_{\mu\nu} = \partial_\nu\vec{\rho}_\mu - \partial_\mu\vec{\rho}_\nu - g_\rho(\vec{\rho}_\mu \times \vec{\rho}_\nu)$. The baryon masses are M_b and the meson masses are m_j. The meson-baryon coupling constants are normally written as $g_{jb} = \chi_{jb}g_j$, where g_j is the coupling of the meson with the nucleon and χ_{jb} is a value obtained according to su(3) symmetry or potential values. These quantities are quite important if hyperons are included in the system and a discussion on their values can be seen in [12] or [17].

The usual steps in a mean field approximation is to treat the meson fields as classical fields and then calculate the equations of motion via Euler-Lagrange equations assuming that the system obeys translational and rotational invariance. Once the equations of motion are solved self-consistently, the energy-momentum tensor is used in the calculation of the EOS. I omit the calculations, which can be easily found in thousands of papers, [8] and [13] among them.

Next, whenever stellar matter is considered, leptons (generally electrons and muons) have to be taken into account because of two extra conditions that have to be imposed, β-equilibrium and charge neutrality. These conditions imply that:

$$\mu_b = \mu_n - q_b\mu_e, \quad \mu_e = \mu_\mu, \quad \sum_b q_b n_b + \sum_l q_l n_l = 0, \tag{11}$$

where μ_b and q_b are the chemical potential and the electrical charge of the baryons, q_l is the electrical charge of the leptons while n_B and n_l are the number densities of the baryons and leptons. In protoneutron stars, before deleptonization, neutrinos have also to be included in the system. When this is done, the chemical stability condition becomes

$$\mu_b = \mu_n - q_b(\mu_e - \mu_{\nu_e}), \quad \mu_e = \mu_\mu. \tag{12}$$

In this case, entropy should be fixed to values compatible with simulations of neutron star cooling and the lepton fractions can reach 0.3-0.4. I do no treat this scenario in the present paper, but examples of this calculation can be seen in [14], as an example.

3.1. Structure of neutron stars

The internal constitution of a neutron star is believed to be known, although it cannot be directly tested. Close to the surface of the star, there is an outer and an inner crust and towards the center, there is also an outer and an inner core. It is widely accepted that the solid crust is formed by nonuniform neutron rich matter in β-equilibrium above a liquid mantle. This inhomogeneous phase, known as pasta phase, can exist at densities lower than 0.1 fm^{-3}. In

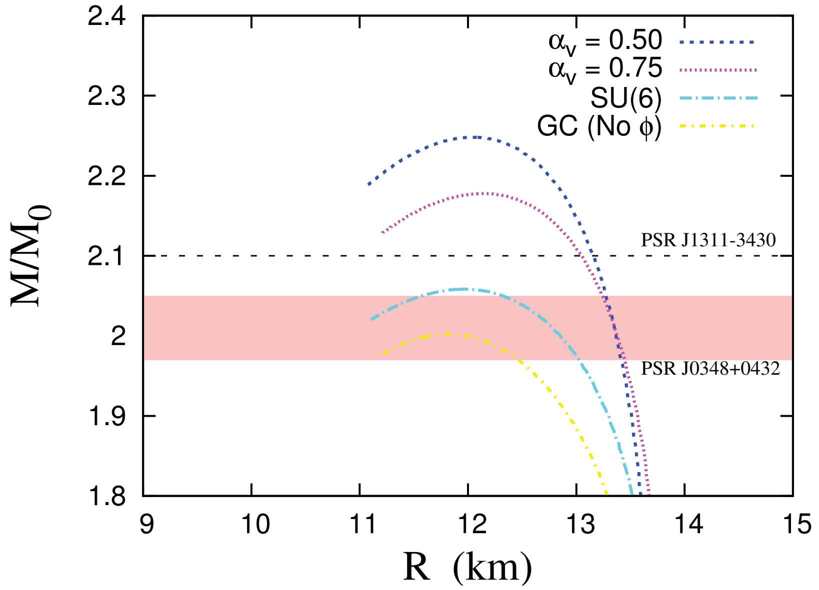

Figure 8. Mass-radius curve for GM1LM parametrization of the non-linear Walecka model. Figure and parametrization taken from [17].

the inner crust nuclei coexist with a gas of neutrons which have dripped out. The center of the star is composed of hadronic matter and the true constituents are still a matter of intense debate. It is a common understanding that the outer core should contain hyperons, although this possibility excludes many EOS that become too soft to explain the existing PSR J1614-2230 and PSR J0348+0432, which are $2M_{\odot}$ mass neutron stars [15]. The constitution of the inner core is more controversial: it can be matter composed of deconfined quarks or perhaps a mixed phase of quarks and hadrons. All these different internal compositions can be obtained with parameter dependent hadronic models. A comprehensive discussion on different aspects of the EOS can be seen in [12]. Here, I only discuss the possible *tuning* of the EOS, currently taking place, as an attempt to describe massive stars.

Until 2010, when the first neutron star with a $2M_{\odot}$ mass was confirmed, most EOS were considered satisfactory if they yielded maximum masses larger than the canonical $1.44M_{\odot}$. It is a well established and understood fact that the inclusion of hyperons makes the EOS softer and then reduces the stellar maximum mass as compared with the nucleons only EOS counterpart. As the appearance of particles with strangeness content is energetically favorable, different possibilities were considered with the purpose of making the EOS stiffer, one of them being the tuning of the unknown meson-hyperon coupling constants. Another clever mechanism to increase the maximum mass of neutron stars with hyperons in their core is to include an additional vector meson that mediates the hyperon-hyperon interaction [16], [17]. This approach has the advantage of not affecting any of the well known nuclear properties, just pushing away the hyperon threshold and suppressing their fraction at high densities. In Fig. 8, mass-radius curves are shown for different coupling constants of the GM1LM parametrization of the non-linear Walecka model [17]. One can see that all choices presented result in quite high maximum masses, satisfying the new massive star constraint.

I next focus on the stellar crust and the pasta phase, considering its relation with the liquid-gas phase transition present in the QCD phase diagram.

3.2. The Pasta phase and liquid-gas phase transitions

The pasta phase is the outcome of the competition between the nuclear and the Coulomb interactions at very low baryonic densities, giving rise to a frustrated system. Frustration is a phenomenon characterized by the existence of more than one low-energy configuration. Normally the Coulomb and nuclear interactions are well separated so that the atomic nucleus presents itself in the binding situation with which everyone is familiar. However, when these two scales are comparable, a variety of complex structures may appear. They are known as droplets, rods and slabs if they are three, two or one-dimensional and their counterparts (bubbles, tubes and slabs) are also possible, meaning that a 3D phase can be denser inside of the new structure (meatball) or outside (Swiss cheese), a 2D phase can be represented by a spaghetti or a penne and a 1D is always lasagna type. The pasta phase becomes the dominant matter configuration if its free energy (binding energy at zero temperature systems) is lower than the corresponding homogeneous phase. The typical densities for its existence lie between 0.01 and 0.1 fm^{-3}, depending on the model, the used parametrization and the temperature [18].

In the search for coexisting phases that give rise to the pasta phase, some points have to be understood with relation to a binary system: according to [20], when one considers phase transitions in multicomponent systems, the number of phases that can coexist is given by $n+2$, where n is the number of conserved charges. Furthermore, more than two phases can coexist if and only if each pair of phases form a a binodal and if all the binodals have a common region of intersection. Based on this criterion, assuming a possibly asymmetric system with two conserved charges and using a Maxwell construction, one gets:

$$\left(\frac{\partial \mu_p}{\partial Y_p}\right)_{T,P} \geq 0 \quad \text{and} \quad \left(\frac{\partial \mu_n}{\partial Y_p}\right)_{T,P} \leq 0, \tag{13}$$

known as diffusive stability, which reflects the fact that in a stable system, energy is required to change the proton concentration while pressure and temperature are kept constant. In the above equations, μ_i, $i = p, n$ is the chemical potential of the proton and neutron and $Y_p = \rho_p/\rho$ is the proton fraction, where ρ_i is the density of protons and neutrons and $\rho = \rho_p + \rho_n$. In order to obtain the binodal section which contains points under the same pressure for different proton fractions, we use the conditions above together with the Gibbs' conditions which impose that both phases have the same pressure and proton and neutron chemical potentials. The pasta phase can then be obtained with different approaches: the coexisting phases (CP) method, the Thomas-Fermi approximation, numerical simulations, etc. For detailed calculations, one can look at [18], [19].

In Fig. 9, a typical case of the comparison of the binding energy of a homogeneous matter with the pasta phase is shown. One sees that the pasta phase binding energy (solid line) is lower up to a certain density, when the homogeneous phase (dashed line) becomes the true preferential state. Different colors represent different structures of the pasta phase. In Fig. 10, different phase diagrams obtained with the CP and TF methods are shown for fixed proton fractions at different temperatures. As the temperature increases, the pasta phase shrinks and the homogeneous phase is also the dominant phase at very low densities, before the onset of the pasta phase. it is worth pointing out that different approximations and different parametrizations result in quite different internal structures and also different transition densities from one phase to another.

For completeness, a binodal section, depicting the regions of phase coexistence with two different relativistic models is shown in Fig. 11.

To conclude this discussion, we briefly outline the importance of studying spinodal sections. The existence of phase transitions from liquid to gas phases in asymmetric nuclear matter (ANM) is related with the instability regions which are limited by the spinodals. The spinodal instability is known to be dominated by density fluctuations which lead to a liquid-gas separation with

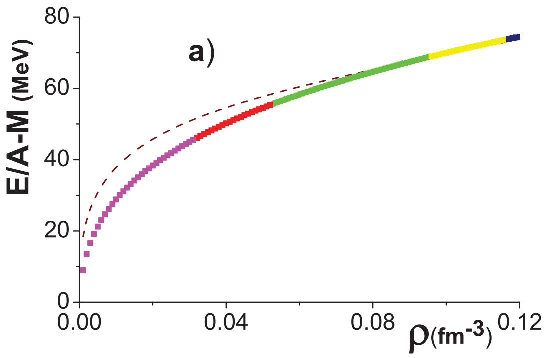

Figure 9. *npe* matter binding energy obtained with the CP method and NL3 parametrization [21]. Figure taken from [18].

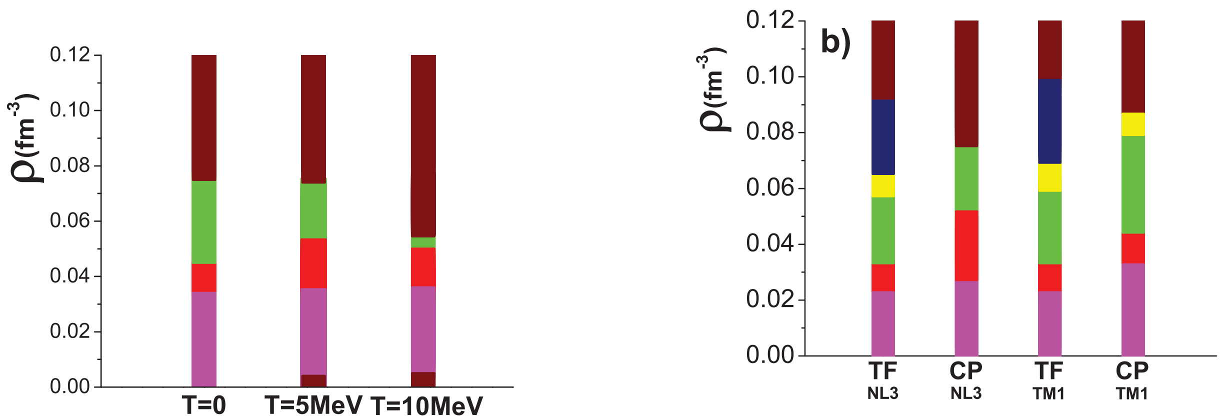

Figure 10. Phase diagrams obtained with a) NL3 [21] parametrization and CP method for $Y_p = 0.5$.From bottom to top the colors represent homogeneous phase (T=5 and 10 MeV only), droplets, rods and homogeneous phase. b)NL3 and TM1 [22] parametrizations with CP and TF methods for $Y_p = 0.3$. From bottom to top the colors represent droplets, rods, slabs, tubes, bubbles and homogeneous phase. Figures taken from [18].

restoration of the isospin symmetry in the dense phase. The stability conditions for asymmetric nuclear matter, keeping volume and temperature constant, are obtained from the free energy density $\mathcal{F}$, imposing that this function is a convex function of the densities ρ_p and ρ_n, i.e. the symmetric matrix with the elements

$$\mathcal{F}_{ij} = \left(\frac{\partial^2 \mathcal{F}}{\partial \rho_i \partial \rho_j}\right)_T, \tag{14}$$

is positive. This corresponds to imposing that the trace and the determinant of the $\mathcal{F}_{ij}$ are positive:

$$\left(\frac{\partial P}{\partial \rho}\right)_{T,Y_p} > 0$$

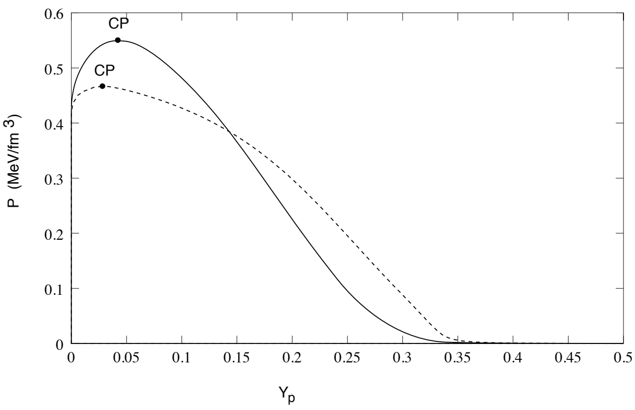

Figure 11. Binodal section for two different relativistic models. CP refers to the critical point.

and

$$\left(\frac{\partial P}{\partial \rho}\right)_{T,Y_p} \left(\frac{\partial \mu_p}{\partial Y_p}\right)_{T,P} > 0, \tag{15}$$

where $\mu_i = \left.\frac{\partial \mathcal{F}}{\partial \rho_i}\right|_{T,\rho_{j\neq i}}$. The spinodal is determined by the values of T, ρ, and Y_p for which the determinant of $\mathcal{F}_{ij}$, (14), goes to zero, i.e. one of the eigenvalues goes to zero and becomes negative in the instability region. The eigenvalues of the stability matrix are given by

$$\lambda_\pm = \frac{1}{2}\left(\mathrm{Tr}(\mathcal{F}) \pm \sqrt{\mathrm{Tr}(\mathcal{F})^2 - 4\mathrm{Det}(\mathcal{F})}\right), \tag{16}$$

and the eigenvectors $\delta\rho_\pm$ by

$$\frac{\delta\rho_i^\pm}{\delta\rho_j^\pm} = \frac{\lambda_\pm - \mathcal{F}_{jj}}{\mathcal{F}_{ji}}, \quad i,j = p,n \tag{17}$$

The largest eigenvalue is always positive and the other becomes negative at the spinodal. In Fig. 12 the spinodal sections for a system of protons and neutrons and for another system also with electrons are shown. The unstable region is defined by the inner part of the spinodal. The inclusion of electrons make matter much more stable. The dashed line represents the results obtained for matter in β-equilibrium. The fact that this curve crosses the spinodal section means that a liquid-gas phase transition occurs at the crust of a cold neutron star, favoring the existence of a non-homogeneous phase.

Finally, in Fig. 13, we compare the results for liquid-gas transition densities for several temperatures, two proton fractions and matter in β-equilibrium obtained with different methods. It is obvious that different methods result in different quantitative results, although all of them agree with the fact that a liquid-gas transition exist, giving rise to a pasta phase structure at low densities. Had we used another parametrization, the numerical results would also be different.

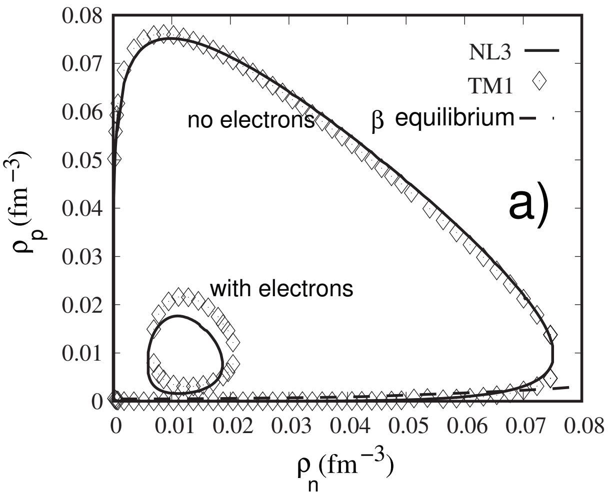

Figure 12. Spinodal section for two parametrizations of the non-linear Walecka model with and without electrons. Figure taken from [23].

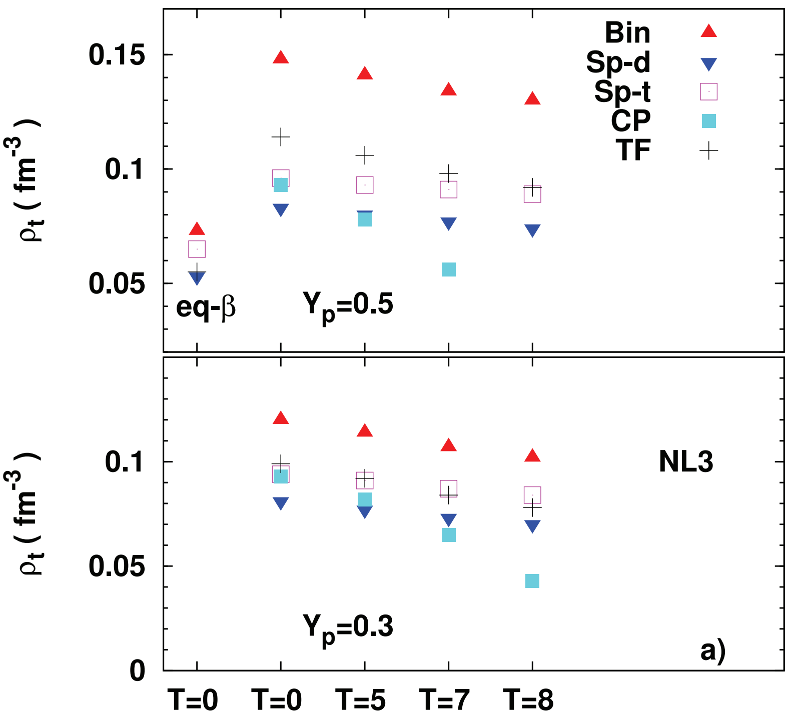

Figure 13. Transition density obtained with the NL3 parametrization [21]. The methods used are: estimation from binodal (Bin), estimation from dynamical spinodal (Sp-d), estimation from thermodynamical spinodal (Sp-th) and pasta phases obtained with the coexistence phases method (CP) and Thomas-Fermi approximation (TF). Figure taken from [24].

4. Relativistic models for heavy ion collisions

As far as heavy ion collisions are concerned, they lie in regions of low chemical potentials and high temperatures in the QCD phase diagram. These temperature and chemical potential are related to the chemical freeze-out regime, which depends on the beam energy. Hadron multiplicities are some of the observables that can give information on the medium from which they are produced. The main facilities running heavy ion collision experiments and the period of data taken were/are:

- AGS, Brookhaven National Laboratory (BNL), from 1986 to 2000, used Au+Au with energy range 2.6 − 4.3 GeV;
- SPS, CERN, from 1986 to 2003, used Pb+Pb with energy range 8.6 − 17.2 GeV;
- RHIC, BNL, started in 2000, uses Au+Au with energies reaching 200 GeV
- LHC, CERN, started in 2009, uses Pb+Pb with energies that will reach 5.5 TeV

As examples, I mention the three types of collisions that take place in the LHC. Proton-proton (**p-p**) collisions are performed so that as much energy as possible are concentrated in the smallest possible volume. The aim is to produce elementary particles with the possible highest masses, as Higgs-like particles. The idea behind the experiments involving lead-lead (**Pb-Pb**) collisions is not to produce new particles, but to understand how the ones already known interact with each other by investigating the properties of the fluid produced in the collision. Finally, proton-lead (**p-Pb**) collisions give the basis to study partonic distribution inside the incoming ion. Comparing the last two reactions, density effects can also be identified.

Both thermal models [25] and quantum hadrodynamical models [26],[27] have been used to calculate hadron multiplicities quite successfully. Some results are shown in Table 1, from where one can see that the freeze-out temperatures and chemical potentials show a small dependence on the different parametrizations. This is due to the fact that the repulsion among the baryons is small and the hadron production is not very sensitive to the hadron-meson interactions. Hence, the meson-hyperon coupling constants play only a very limited role.

5. Final remarks

I have tried to show how different aspects of the QCD phase diagram can be investigated with the help of parameter dependent hadronic models. Two regions of the QCD phase diagram have received special attention: the region of low temperature and high baryonic density, where neutron stars are a source of intense investigation and the region of low baryonic densities and high temperature, represented by the physics taking place in heavy ion collisions.

Other important aspects could also be discussed, as the possible existence and location of the critical end point (CEP) [28], where the first order transition line shown in Fig. 5 ends. This is an important topic of recent research. LQCD forsees a crossover transition for the low density part of the QCD phase diagram, starting from a point with zero chemical potential and high temperature. Effective models, on the other hand, give a first order phase transition starting at a zero temperature and high density point. If these curves are to be joined, a CEP is necessary. If this point does not exist, as advocated my some LQCD results, then the transition would be of the crossover type all the way down and as a consequence, all calculations involving hadron-quark phase transitions as the ones in the interior of hybrid stars would have to be revisited or even ruled out.

It is obvious, from the results presented and discussed, that they are almost always parameter dependent, what means that their interpretation has to be taken with some care. However, although one cannot guarantee that the quantitative results are accurate, the knowledge on the physics has been greatly improved with the help of effective models. As far as physical constraints are obeyed so that we have some control of the parameters used in different models,

Ratio	GM3 set 1	GM3 set 2	Free	Exp. Data	Exp.
$\bar{p}/p$	0.671	0.674	0.674	0.65±0.07	STAR
				0.64±0.07	PHENIX
				0.60±0.07	PHOBOS
				0.64±0.07	BRAHMS
$\bar{p}/\pi^-$	0.046	0.045	0.038	0.08±0.01	STAR
π^-/π^+	1.005	1.005	1.004	1.00±0.02	PHOBOS
				0.95±0.06	BRAHMS
K^-/K^+	0.958	0.960	0.964	0.88±0.05	STAR
				0.78±0.13	PHENIX
				0.91±0.09	PHOBOS
				0.89±0.07	BRAHMS
K^-/π^-	0.238	0.236	0.231	0.149±0.02	STAR
K^{*0}/h^-	0.063	0.062	0.059	0.06±0.017	STAR
$\bar{K}^{*0}/h^-$	0.060	0.059	0.057	0.058±0.017	STAR
$\bar{\Lambda}/\Lambda$	0.696	0.698	0.699	0.77±0.07	STAR
Ξ^+/Ξ^-	0.726	0.717	0.725	0.82±0.08	STAR
T (MeV)	148.3	147.7	145.7		
μ_B (MeV)	32.24	31.60	28.88		
χ^2_{dof}	5.71	5.83	6.24		

Table 1. Comparison of experimental particle ratios with the ones obtained from the relativistic mean-field models used in this work for two different meson-hyperon couplings, together with the chemical freeze-out temperature T, baryonic potential μ_B and χ^2_{dof}. Also shown are the results obtained from a free gas (Free). These results were taken from [27].

there is no doubt that these models remain a valuable tool in undestanding many physical aspects of nature.

5.1. Acknowledgments

I would like to thank the organizers of the XIII Hadron Physics meeting, namely, Marcelo Chiapparini, Mirian Bracco and Marina Nielsen for the invitation to prepare and give the Colloquium, a very challenging but pleasant task. I am partially supported by Conselho Nacional de Desenvolvimento Científico e Tecnológico (CNPq-Brazil) and by Fundação de Amparo à Pesquisa e Inovação do Estado de Santa Catarina (FAPESC), under project 2716/2012.

References

[1] Hoelbing C (2014) arXiv:1410.3403[hep-ph]; Lepage G P (2005) arXiv:hep-lat/0506036.
[2] Mackie F D and Baym G 1977 *Nucl. Phys.* A **285** 332.
[3] von Weizscker 1935 *Zeitschrift fr Physik* **96 (78)** 431.
[4] Avancini S S, Marinelli J R, Menezes D P , Moraes M M W and Schneider A S 2007 *Phys. Rev.* C **76** 064318.
[5] Menezes D P 2002 *Intordução à Física Nuclear e de Partículas Elementares* (Florianópolis: Editora da UFSC)
[6] Krane K S (1988) *Introductory Nuclear Physics* (New York: John Wiley and Sons, Inc.)
[7] Dutra M, Lourenço O, Sá Martins J S, Delfino A, Stone J R, and Stevenson P D (2012) *Phys. Rev.* C **85**, 035201.
[8] Dutra M, Lourenço O, Avancini S S , Carlson B v, Delfino A, Menezes D P, Providencia C, Typel S and Stone J R (2014) *Phys. Rev.* C **90**, 055203.
[9] Li B-A and Han X (2013) *Phys. Lett.* B **727**, 276.

[10] Oppenheimer J R, Volkoff G M (1939) *Phys. Rev.* **55**, 374.
[11] http://compose.obspm.fr
[12] Glendenning N K (2000)*Compact Stars* (New York: Springer).
[13] Walecka J D (1974) *Ann. Phys.* **83**, 491; Serot B and Walecka J D (1986) *Advances in Nuclear Physics* **16**.
[14] Menezes D P and Providência C (2004) *Phys. Rev.* C **69** 045801; Panda P K, Menezes D P and Providência C (2004) *Phys. Rev.* C **69** 058801.
[15] Demorest B et al (2010) *Nature* **467**, 1081; Antoniadis J et al (2013) *Science* **340** 1233232.
[16] Weissenborn S, Chatterjee D, Schaffner-Bielich J (2012) *Nucl. Phys.* A **881** 62; Weissenborn S, Chatterjee D, Schaffner-Bielich J (2012) *Phys. Rev.* C **85**, 065802.
[17] Lopes L L and Menezes D P (2014) *Phys. Rev.* C **89** 025805.
[18] Avancini S S, Menezes D P, Alloy M D, Marinelli J R, Moraes M M W and Providência C (2008) *Phys. Rev.* C **78**, 015802.
[19] Maruyama T, Tatsumi T, Voskresensky D N, Tanigawa T and Chiba S, *Phys. Rev.* C **72**, 015802.
[20] Müller H and Serot B (1995) *Phys. Rev.* C **52** 2072.
[21] Lalazissis G A, König J and Ring P (1997) *Phys. Rev.* C **55**, 540.
[22] Sumiyoshi K, Kuwabara H and Toki H (1995) *Nucl. Phys.* A **581** 725.
[23] Avancini S S, Brito L, Chomaz Ph, Menezes D P and Providência C (2006) *Phys. Rev.* C **74**, 024317.
[24] Avancini S S, Chiacchiera S, Menezes D P and Providência C (2012) *Phys. Rev.* C **85**, 059904(E).
[25] Braun-Munzinger P, Heppe I and Stachel J (1999) *Phys. Lett.* B **465** 15; Braun-Munzinger P, Magestro D, Redlich K and Stachel J (2001) *Phys. Lett.* B **518** 21.
[26] Menezes D P, Providência C, Chiapparini M, Bracco M E, Delfino A and Malheiro M (2007) *Phys. Rev.* C **76**, 064902.
[27] Chiapparini M, Bracco M E, Delfino A, Malheiro M, Menezes D P and Providência C (2009) *Nucl. Phys.* A **826** 178.
[28] Costa P, Ferreira M, Hansen H, Menezes D P, Providncia C (2014) *Phys. Rev.* D **89**, 056013.